Gigantic vortical differential scattering as a monochromatic probe for multiscale chiral structures

Jincheng Ni[a,b] , Shunli Liu[a], Dong Wu[a,1], Zhaoxin Lao[a], Zhongyu Wang[a], Kun Huang[c,1] , Shengyun Ji[a], Jiawen Li[a] , Zhixiang Huang[d] , Qihua Xiong[e], Yanlei Hu[a,1], Jiaru Chu[a], and Cheng-Wei Qiu[b,1]

[a]Chinese Academy of Sciences Key Laboratory of Mechanical Behavior and Design of Materials, Department of Precision Machinery and Precision Instrumentation, University of Science and Technology of China, 230027 Hefei, China; [b]Department of Electrical and Computer Engineering, National University of Singapore, 117583 Singapore, Singapore; [c]Department of Optical Engineering, University of Science and Technology of China, 230026 Hefei, China; [d]Key Laboratory of Intelligent Computing and Signal Processing (Ministry of Education), Anhui University, 230039 Hefei, China; and [e]Division of Physics and Applied Physics, School of Physical and Mathematical Sciences, Nanyang Technological University, 637371 Singapore, Singapore

Spin angular momentum of light is vital to investigate enantiomers characterized by circular dichroism (CD), widely adopted in biology, chemistry, and material science. However, to discriminate chiral materials with multiscale features, CD spectroscopy normally requires wavelength-swept laser sources as well as wavelength-specific optical accessories. Here, we experimentally demonstrate an orbital-angular-momentum-assisted approach to yield chiroptical signals with monochromatic light. The gigantic vortical differential scattering (VDS) of ~120% is achieved on intrinsically chiral microstructures fabricated by femtosecond laser. The VDS measurements can robustly generate chiroptical properties on microstructures with varying geometric features (e.g., diameters and helical pitches) and detect chiral molecules with high sensitivity. This VDS scheme lays a paradigm-shift pavement toward efficiently chiroptical discrimination of multiscale chiral structures with photonic orbital angular momentum. It simplifies and complements the conventional CD spectroscopy, opening possibilities for measuring weak optical chirality, especially on mesoscale chiral architectures and macromolecules.

optical chirality | orbital angular momentum | chiral structure | vortex beam

The total angular momentum of massless photons can be divided into spin angular momentum (SAM) and orbital angular momentum (OAM) (1). More than 100 y ago, Poynting (2) reasoned that the SAM, defined as $\mathbf{S} = \pm\hbar$ ($\hbar$ is the reduced Planck constant), is related to the left- and right-handed circular polarizations. However, only nearly three decades ago, Allen et al. (3) recognized that the OAM of light is carried by a paraxial Laguerre–Gaussian beam with a helical wavefront. The photonic OAM can be evaluated by $\mathbf{L} = \ell\hbar$, where the integer ℓ stands for the topological charge and its sign indicates the handedness of helical wavefront. The orthonormal OAMs with unbounded values have been extensively used in optical tweezers (4), optical communications (5), and sensing (6).

On the other hand, chirality, which describes the symmetry property of an object, is quite ubiquitous in nature. A chiral object cannot be superposed with its mirror by rotations or translations, such as hands, DNA, proteins, seashells, or spiral staircases (7). Discriminating the chirality of enantiomers always embraces great opportunities in the pharmaceutical industry in that their handedness is associated with potency and toxicity (8). Apart from direct observation of geometric features, three-dimensional contour of chiral structures can also be probed via a different optical response to left- and right-handed circularly polarized light (7, 9). The chiroptical response in terms of a polarization-dependent extinction coefficient is called circular dichroism (CD), which has been a powerful tool to investigate chiral molecules in biology, chemistry, and material science. Yet, most natural chiral molecules possess extremely weak CD signals because the dimensions of chiral molecules are much smaller than the wavelength-scale helical pitch of circularly polarized

light (10). Several approaches have been proposed to enhance the CD signals by matching the dimensions of chiral materials and the helical pitch of circularly polarized light, such as nanophotonic structures (11), plasmonic nanoparticles (12–14), chiral metamaterials (9, 15), and superchiral light (16). The CD spectroscopy using SAM of light normally requires wavelength-swept laser sources and assorted optics to discriminate multiscale chiral materials. For example, in order to detect the optical chirality of structures with sizes ranging from 10 to 20 μm, one may need to achieve CD signals in the terahertz region with well-designed components—kirigami polarization modulators—for modulation of circular polarizations (17).

The OAM of light has been proposed as an alternative approach to probe the optical chirality of microscopic objects (18). Unfortunately, the attempt to directly detect optical chirality of molecules by using the photonic OAM has negligible results in a long period (19, 20). Even with unique plasmonic nanoparticle aggregates to excite the electric quadrupole fields, such an indirect approach still leads to a weak chiroptical signal of ~0.6% (21). To date, in comparison with CD signals, the pronounced chiroptical signals via photonic OAM have remained unseen.

Here, we theoretically propose and experimentally demonstrate a gigantic chiroptical response of vortical differential scattering (VDS) arising from the strong interaction between intrinsically chiral microstructures and OAM beams. We experimentally obtain the maximum VDS of ~120% by matching the OAM beams with the dimensions of chiral microstructures (Fig. 1A). The dependence of VDS response on the dimensions

Significance

Optical chirality by light–matter interaction is a powerful strategy for discriminating the chirality of materials in modern physics. Here we present a vortex-dependent approach to yield a direct chiroptical response with monochromatic light. The chiroptical signal of ~120% is obtained on intrinsically chiral microstructures by optical vortices in the visible range. The chiroptical properties of microstructures can be flexibly controlled by tuning their geometric features. We further demonstrate the strong chiral light–matter interaction by optical vortices for sensitively detecting optical chirality of molecules.

APPLIED PHYSICAL SCIENCES

Fig. 1. (*A* and *B*) Schematics of the interaction between chiral structures and light beams with OAM and SAM, respectively. (*A*) VDS induced by vortex beams with helical phase wavefronts locates at the dimensional matching between vortex beams and chiral structures ($D > \lambda$). (*B*) CD induced by circularly polarized light with helical electric field vectors is normally at the dimensions of chiral structures comparable or smaller than the wavelength λ ($D < \lambda$). (*C*) Comparative overview of the CD and VDS response zones. Pink dots represent the resonant peaks of CD spectra found in previous literature (9, 12, 22–27); the black line indicates that D is equal to λ; the blue dots represent the results of VDS obtained in our work. (*D*) The dimensional matching between chiral structures and chiral light (with SAM or OAM) for yielding strong chiroptical signals. (*E*) Illustration of the OAM beam with helical wavefront illuminating on the chiral structure at normal incidence. The Poynting vector (green arrow) of the OAM beam screws around the beam axis with a helix angle of θ. The chiral structure has a lead angle of α. The chiral VDS interactions demonstrate the mirror-symmetric property by changing their handedness from (θ, α) to ($-\theta$, $-\alpha$).

of chiral structures has also been investigated, exhibiting a robust chiroptical behavior beyond the regions explored by conventional CD responses. Our proposed concept also demonstrates the capability of sensitively detecting chiroptical signals of molecules with OAM beams in the visible wavelength range.

Results

Principles of Strong VDS Effects by OAM Beams. CD spectroscopy, utilizing photonic SAM, generally exhibits a strong chiroptical signal by matching the structural dimension and wavelength (12), as shown in Fig. 1*B*. We can understand the CD and VDS properties on dimensions of chiral structures in an intuitive diagram (Fig. 1*C*). The resonant wavelengths of chiral structures on CD spectroscopy are red-shifted with larger diameters (9, 12, 22–27) but usually still confined in the chiroptical-response zone of $D < \lambda$. The well-established wavelength-dependent paradigm is inconvenient, especially for detecting the chiroptical properties of multiscale chiral structures. To break through the limited zone of chiroptical response, OAM beams are introduced as the detecting light. Distinguishing from the wavelength-scale chiral information in circularly polarized light, the chiral properties of OAM beams are contained in the helical wavefronts. Therefore, the designed chiral structures in our experiments have sizes comparable to the beam waist for dimensional matching (Fig. 1*D*). This implies that the VDS spectra are generated at the dimensions of chiral microstructures larger than the operating wavelength, locating in the unexplored zone of $D > \lambda$. In particular, by introducing the unbounded topological charges of vortex beams as a new degree of freedom, the VDS measurements can even be achieved at the same wavelength (i.e., $\lambda = 800$ nm in our experiments), yielding a three-dimensional response zone of optical chirality.

As shown in Fig. 1*E*, vortex beams impinge on the chiral structure for VDS measurements. Compared to the linear energy

flux of a plane wave, the Poynting vector of optical vortex follows a spiral trajectory twisted around the beam axis (28). Hence, at a certain radial position r of the vortex beam, the helix angle between its Poynting vector and optical axis can be recorded as θ and $-\theta$ for right- and left-handed helical wavefronts, respectively. Furthermore, the chiral structure has a lead angle of $\alpha = \pm\tan^{-1}[H/(2\pi r)]$, where H is its helical pitch, r is its radial position, and its sign indicates the handedness of structure. Considering the parity-odd scalar of chirality (16), the scattering intensity is invariant by flipping the helicity of vortex beam and structure simultaneously, resulting in the mirror-symmetric property of VDS spectra (*SI Appendix*, Fig. S1).

Measurement of Gigantic VDS. To exclude the conventional CD effect, linearly polarized vortex beams were used in our experiments. The interaction between vortex beams and chiral microstructures can be obtained by measuring the diverse scattering intensity as a function of topological charges ℓ. Chiral microstructures in analog of spiral staircases were fabricated in polymer resist SZ2080 by direct laser writing. The left- and right-handed microstructures have a diameter $D = 17.4$ μm, helical pitch $H = 21.4$ μm, and thickness $t = 2.2$ μm. An achiral cylindrical microstructure was also fabricated as a reference sample. The chiral and achiral microstructures with the same diameter are closely related from the top-down view (*SI Appendix*, Fig. S2). Illuminating on the left- and right-handed microstructures by optical vortices, the scattering spectra are split for opposite topological charges $|\ell|$ ranging from 5 to 65, as shown in Fig. 2 *A* and *B*. As a control experiment, the scattering spectrum of achiral microstructure illuminated by optical vortices does not show any pronounced features (Fig. 2*C*). Moreover, the polarization-independent scattering spectra on chiral structures are also observed by circularly polarized vortex beams (*SI Appendix*, Fig. S3).

Ni et al.
Gigantic vortical differential scattering as a monochromatic probe for multiscale chiral structures
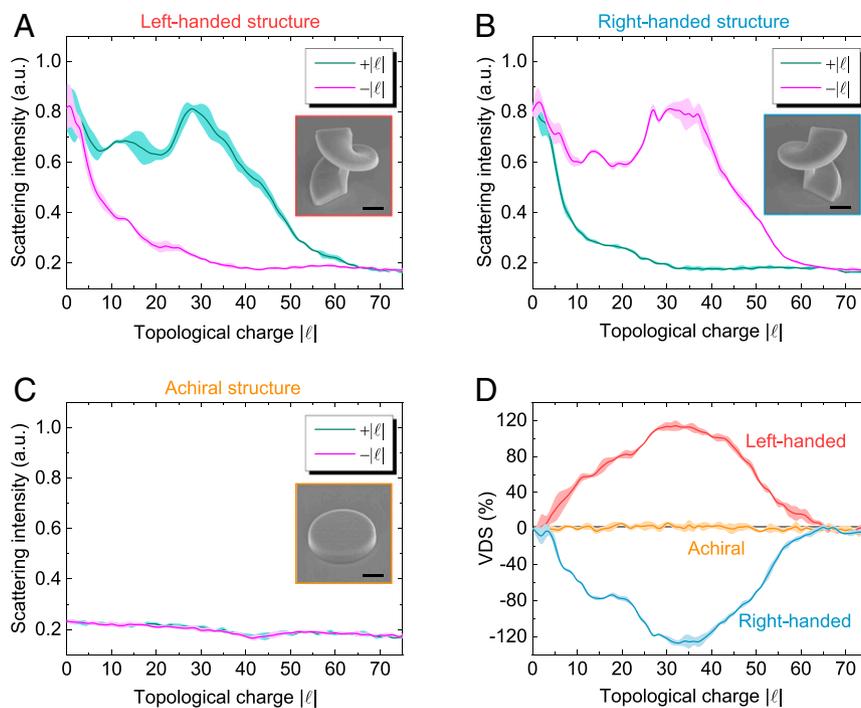
Fig. 2. (*A–C*) The measured scattering intensity on left-handed, right-handed, and achiral microstructures illuminated by optical vortices with different topological charges. (*Insets*) The SEM images of corresponding microstructures by direct laser writing in the polymer SZ2080. a.u.: arbitrary units. (Scale bars, 5 μm.) (*D*) VDS spectra of the chiral and achiral microstructures. The gray straight line indicates VDS = 0 for a guide to the eye. Each solid line shows the mean value and the shading indicates their SD of multiple measurements.

In a fashion similar to Kuhn's *g*-factor (29–31) for CD assessments, we can define the VDS by the following dissymmetry factor as

$$VDS = \frac{I_{+|\ell|} - I_{-|\ell|}}{(I_{+|\ell|} + I_{-|\ell|})/2} \times 100\%, \qquad [1]$$

where $I_{+|\ell|}$ and $I_{-|\ell|}$ are the scattering intensity under the illumination of optical vortices with topological charge $+|\ell|$ and $-|\ell|$, respectively. Fig. 2*D* shows that the left-handed microstructure produces a VDS signal with a characteristic peak at $|\ell| \sim 32$, while the right-handed microstructure produces a vertically mirrored VDS signal (*SI Appendix*, Table S1). Note that both VDS spectra are convergent to near-zero values after exceeding the resonant area with $|\ell| > 65$. In general, the chiroptical responses of left- and right-handed microstructures are mirror images with respect to the zero line, where the VDS spectrum of achiral microstructure is located. Analogous to conventional CD spectra, the VDS clearly distinguishes the intrinsic handedness of structures, which is also confirmed by the theoretical simulations (*SI Appendix*, Fig. S4). By photonic SAM, the corresponding circular differential scattering (CDS) measurements of chiral microstructures have negligible results owing to the nonresonant operating wavelength (*SI Appendix*, Fig. S5). Nonetheless, the maximum VDS value of ~120% is still significant and can clearly discriminate their optical chirality. In addition, it is worth noting that the conventional CD normally requires plenty of analytes or arrayed chiral metasurfaces for yielding a distinct chiroptical signal (32), whereas the VDS in our configuration is implemented directly by only a single chiral structure.

Experimental Setup for Measuring VDS Spectra. The optical setup for measuring VDS spectra is depicted in Fig. 3*A*. A fundamental-mode Gaussian beam at the wavelength of 800 nm was used in our experiments and then collimated to illuminate a fork

hologram on a liquid-crystal spatial light modulator (SLM). In order to separate the first-order vortex beam, a tilted shift phase was added to the azimuthal phase hologram that has ℓ phase cycles around the axis. A 4*f* system with an iris located at the confocal plane was employed to filter out undesired orders of diffraction. The well-prepared vortex beam was finally focused by a 100× objective lens to generate a donut-shaped optical field, and the sample was irradiated at normal incidence to avoid introducing extrinsic chirality from light. The sign of topological charge ℓ of the vortex beam is reversed after three reflections upon mirrors (33).

Experimentally, the optical field distributions of vortex beams at the focal plane are captured by a charge-coupled device (CCD) camera, as shown in Fig. 3*B*. The slightly directional distributions on the intensity profiles are induced by linearly polarized state of light beam, which does not influence the polarization-independent VDS measurements. The intensity profiles of focused vortex beams can be simulated by the vectorial Debye diffraction theory (see *Materials and Methods* for further details). As the E_z component is undetectable in objective-based optical microscopy (34), we only consider the intensity and phase distributions of transverse components. The optical vortices with opposite topological charges $\pm|\ell|$ theoretically have the same transversal intensity distributions but opposite azimuthal phase gradients. The diameter d of the ring profile is defined as the distance between two peaks on the cross-section of optical fields. Fig. 3*C* shows that the experimental diameter d of the focused vortex beam increases linearly with topological charge $|\ell|$, which is consistent with the predicated $|\ell|$ scaling law under focused condition (35) (see *SI Appendix*, Note S3 for more details on the linear function). The numerically simulated intensity distributions of optical vortices are in excellent agreement with the experimental results (*SI Appendix*, Fig. S6).

The linear variation of vortex-beam diameter unveils the generation of chiroptical signals on VDS spectra. When the donut-shaped

Ni et al.
Gigantic vortical differential scattering as a monochromatic probe for multiscale chiral structures

PNAS | 3 of 7
https://doi.org/10.1073/pnas.2020055118

APPLIED PHYSICAL SCIENCES
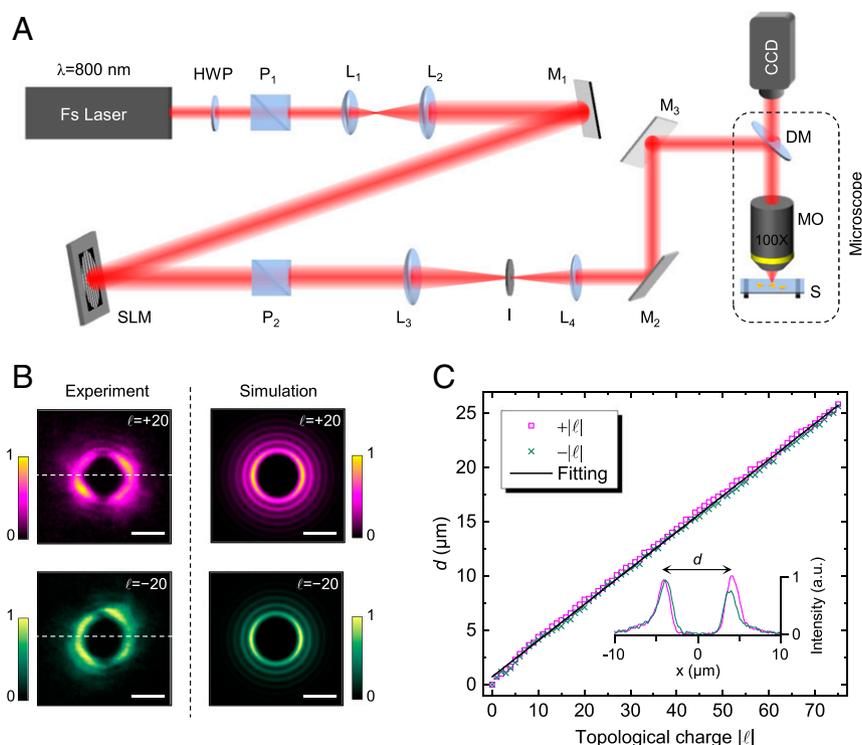
Fig. 3. (*A*) Experimental apparatus for measuring VDS spectra. A femtosecond laser is expanded by a telescope (lenses L_1 and L_2) to match the size of SLM, after its polarization and power adjusted by a half-wave plate (HWP) and a polarizer (P_1). The linearly polarized Gaussian light beam is modulated by the SLM after reflecting from a mirror (M_1). The desired vortex beam at the first-order diffraction is selected by an iris (I) and then introduced into a microscope system. After that, the vortex beam is focused on the sample (S) by a 100× microscope objective (MO). Finally, the scattering intensities are recorded by a CCD camera. DM, dichroic mirror. (*B*) Measured and simulated intensity profiles on the focal plane with topological charges $\ell = +20$ (*Top*) and -20 (*Bottom*). (Scale bars, 5 µm.) (*C*) Measured diameter d of the vortex beam as a function of topological charge. The solid line represents the linear fitting of measured diameter d. (*Inset*) The line plots of measured intensity profiles in *B*.

profiles of vortex beams enlarge with the increment of topological charge $|\ell|$, the VDS of the left-handed (right-handed) microstructure increases from zero to its maximum (minimum) value with the strong resonance, as shown in Fig. 2*D*. The VDS value decreases to near-zero when the donut-shaped profile is larger than the diameter of chiral microstructure, which implies a weak interaction between vortex beams and chiral structures. Intuitively, the optical scattering profiles also provide a straightforward illustration for the chiroptical VDS generation (*SI Appendix*, Fig. S7).

Chiroptical Properties on Geometric Parameters by Monochromatic VDS. To further elucidate the chiroptical properties of VDS, we experimentally investigate the VDS responses of chiral microstructures under different diameter D and helical pitch H. First, the resonant peak of the VDS spectrum is shifted by changing diameter D of chiral microstructures. We measured the VDS signals on left-handed microstructures with a fixed helical pitch $H = 21.4$ µm but varying diameter D from 11.5 µm to 21.2 µm, as shown in Fig. 4*A*. As the diameter D increases, the resonant peak of VDS spectra gradually shifts toward larger topological charge $|\ell|$, further confirming the dimension-matching concept between chiral structures and vortex beams. When donut-shaped profiles of optical vortices with large topological charges $|\ell|$ exactly deviate from the chiral microstructures, the VDS regresses to near-zero values, defined as critical points in VDS spectra (*SI Appendix*, Fig. S8). Considering the linearly variant diameters of vortex beams, the shift positions of critical points show a linear relationship with D, as shown in Fig. 4*B*. Intriguingly, although the experiments are implemented by using chiral microstructures with different D, the maximum VDS values almost keep the same magnitude of ~120%. Second, the helical pitch H of chiral

microstructures determines the lead angle α, which significantly influences the maximum VDS values. Fig. 4*C* depicts the VDS spectra of left-handed microstructures with a fixed diameter $D = 17.3$ µm but varying helical pitch H from 11.3 µm to 31.4 µm. Among these chiral microstructures, the maximum VDS is located at $H = 21.4$ µm, where a strong chiral light–matter interaction occurs by matching the helical pitches between the structures and vortex beams. However, the critical points maintain at $|\ell| = 60$ because of the fixed diameter D, as shown in Fig. 4*D*. The analyses of VDS spectra can shed light on the design mechanism of chiral structures and prediction of their intrinsically chiroptical properties by vortex beams.

Detecting the Optical Chirality of Molecules via VDS. Benefitting from the strong chiral light–matter interaction with the dimension-matching concept, the CD-relative chiroptical techniques with photonic SAM can also be extended to the VDS regime. For example, in CD measurements, locally enhanced chiral fields on artificial structures generated by circularly polarized light have been widely utilized to enhance the chiroptical signals of chiral molecules at visible wavelengths (8, 15, 36, 37). Although the vortex beams cannot directly interact with chiral molecules with electric or magnetic dipole transitions, the photonic OAM can still probe chiral molecules via electric quadrupole transitions (21). After plasmon coupling with structures, the excited electric quadrupole transitions lead to the chiroptical effects of molecules with photonic OAM (38, 39). Analogous to the situations of circularly polarized light, electromagnetic fields with locally enhanced optical chirality are also formed in the near field of chiral microstructures by optical vortices, confirmed by the theoretical simulations (*SI Appendix*, Fig. S9).
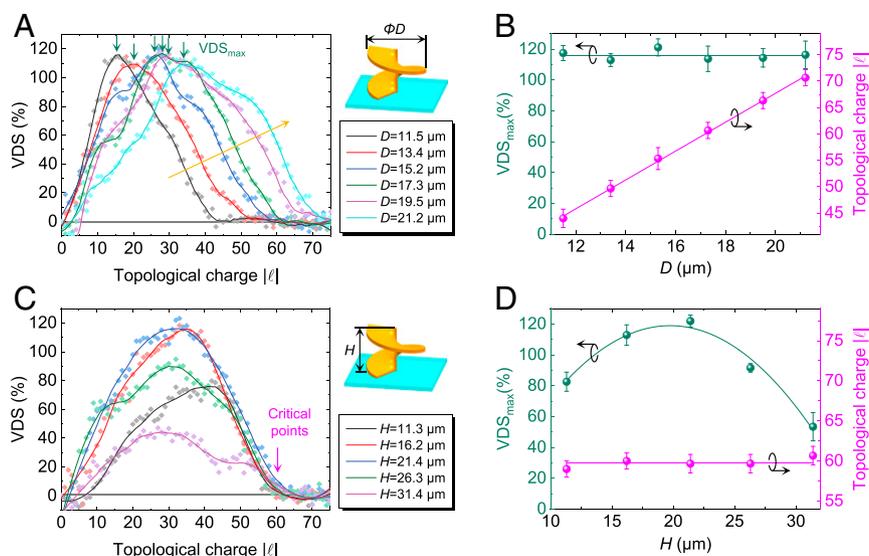
Fig. 4. (*A*) Measured VDS spectra of chiral microstructures with the fixed helical pitch $H = 21.4$ μm but different diameter D from 11.5 to 21.2 μm. The yellow arrow indicates the increase of diameter D and green arrows indicate the maximum VDS values. The VDS spectra are right-shifted by increasing the diameter D of chiral microstructures. (*B*) Measured maximum VDS values (green dots) and topological charge $|\ell|$ of critical points (magenta dots, defined in *C*) for different D. (*C*) Measured VDS spectra of chiral microstructures with the fixed diameter $D = 17.3$ μm but different helical pitch H from 11.3 to 31.4 μm. Critical points indicate that VDS values exactly return to zero. (*D*) Measured maximum VDS values and topological charge $|\ell|$ of critical points for different H. The curves are drawn as a guide to the eye. Error bars are the SD of multiple measurements.

We experimentally detected the optical chirality of two en-antiomers (L- and D-phenylalanine) by immersing chiral microstructures in the solutions of molecules and then measured the VDS spectra of the whole system (*SI Appendix*, Fig. S10). The sample with chiral microstructures was coated with a 10-nm Au layer for boosting the scattering in solutions (*SI Appendix*, Fig. S11). Moreover, the thin Au layer on the surface of microstructures can also absorb the chiral molecules with well-defined orientation for chiral light–matter interactions (15, 40). In order to extract the VDS spectra of molecules from the total VDS spectra, we measured the VDS spectra of chiral microstructures in deionized water as the background reference. Then, we collected the VDS spectra of chiral microstructures in L- and D-phenylala-nine solution with femtomolar sensitivity, respectively (Fig. 5 *A* and *B*). To remove the background VDS signals of chiral microstructures (8), the summation of VDS is defined as

$$\Sigma \text{VDS} = \left(\text{VDS}_E^L + \text{VDS}_E^R \right) - \left(\text{VDS}_O^L + \text{VDS}_O^R \right), \quad [2]$$

where VDS_E^L and VDS_E^R are the VDS spectra of left- and right-handed microstructures in enantiomer solution and VDS_O^L and VDS_O^R are the VDS spectra of left- and right-handed microstructures in deionized water, respectively. After this postprocessing, the chiroptical ΣVDS spectra are taken as the VDS signals only from chiral molecules, as shown in Fig. 5*C*. The little difference in the magnitude of the two enantiomers is attributed to the imperfect fabrication of chiral structures and measuring errors. Compared with the CD measurements at the range of 1 to 14% (8, 15), the optical chirality of molecules can be enhanced by detecting the ΣVDS signal of ~25% on the three-dimensional chiral microstructures at the visible wavelength. The simulated and experimental results verify that the locally enhanced chiral fields generated by photonic OAM can also sensitively detect chiral molecules.

Discussion

Given the different dimension-matching concept between photonic SAM and OAM, the chiroptical response of artificial micro/nanostructures and molecules can be extremely extended via VDS

measurements in theory and experiment. First, the VDS response is pronounced by matching the dimensions of chiral structures and OAM beams. For example, to detect the chiroptical properties of structures with large sizes (11.5 to 21.2 μm), the CDS measurements normally need long-wavelength light (21.7 to 31.4 μm), which requires infrared laser sources and assisted waveplates (*SI Appendix*, Fig. S12). However, we can also conveniently achieve the optical chirality from VDS spectra only by using the visible-wavelength laser, as shown in Table 1. Second, compared to SAM with only two states, the theoretically unlimited OAM values provide another flexible and accessible (by using a reconfigurable SLM) avenue for detecting the optical chirality of structures with monochromatic instead of broadband laser. Moreover, our finding that the strong resonance of VDS appears at matching the dimensions of vortex beams and structures explicitly confirms the dimension-matching concept in chiral light–matter interaction. Third, by generating a locally enhanced chiral field, the proposed VDS spectroscopy can also demonstrate the optical chirality of molecules, which may excite a plethora of applications in chiroptical detection of enantiomers. Although the shape of the VDS line as a function of OAM values remains elusive and needs to be further investigated, the optical chirality generated by photonic OAM can predominately improve the chiroptical response in light–matter interactions. Utilizing the dimension-matching concept, more chiroptical effects by vortex beams can also be implemented by mimicking the conventional CD measurement, such as its counterpart-vortical dichroism.

In conclusion, we have observed giant chiroptical VDS signals from intrinsically chiral microstructures induced by optical vortices with topological charge ℓ from −75 to +75. The strong VDS feature of ~120% shows a significant chiroptical response between vortex beams and femtosecond-laser-fabricated microstructures with the dimension-matching concept. The VDS measurements can robustly detect the optical chirality of structures with varying geometric characteristics, such as diameter and helical pitch. Moreover, the locally superchiral fields on chiral microstructures by optical vortices can enhance the chiroptical signals of molecules down to femtomole levels. Our results prove that the response
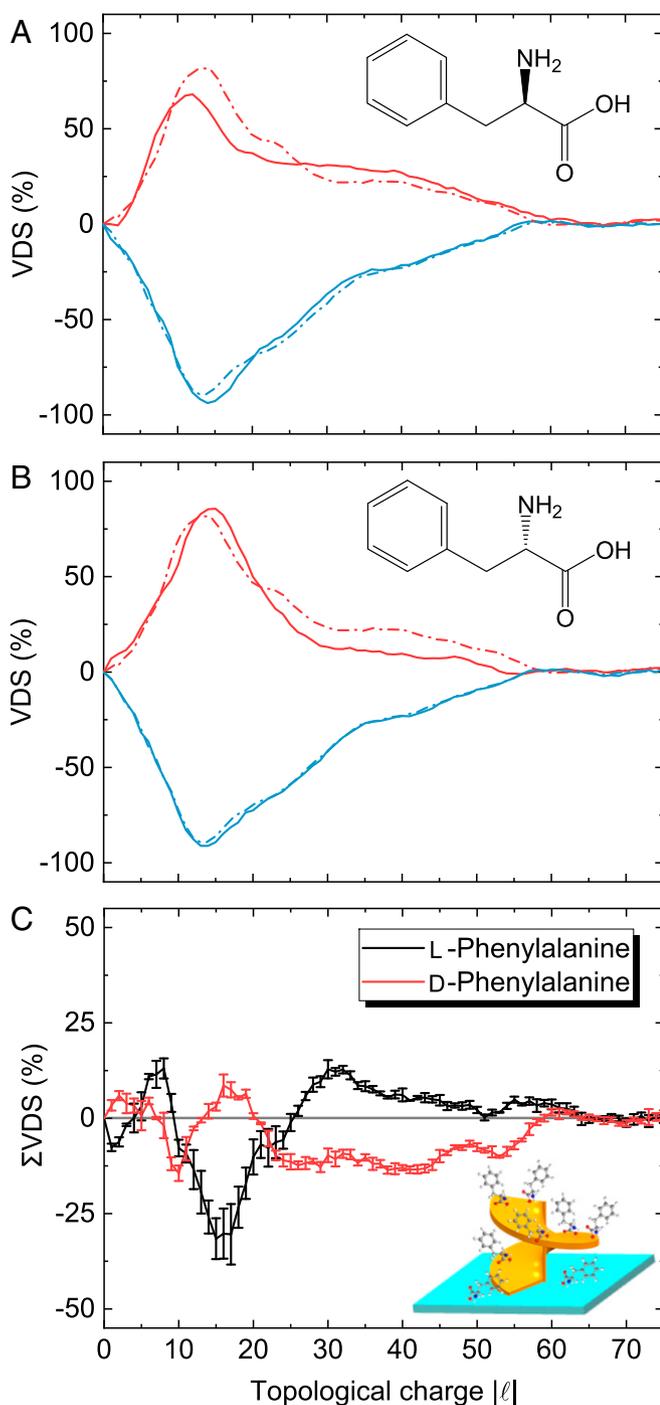
Fig. 5. (*A*) VDS measurements of left- (red) and right-handed microstructures (blue) in deionized water (dashed lines) and L-phenylalanine solution (solid lines), respectively. (*B*) VDS measurements in deionized water (dashed lines) and D-phenylalanine solution (solid lines), respectively. (*C*) VDS summation after removing the background VDS values of chiral microstructures. Error bars indicate the SD of multiple measurements. (*Inset*) The not-to-scale schematic plot of enantiomers sensing with chiral microstructures.

zone of optical chirality can be significantly expanded by the VDS spectra for complementing conventional CD spectra. This technology offers an innovative method to discriminate the optical chirality of micro/nanostructures by using photonic OAM and potentially benefits the wide chirality-related areas across chemistry, biomaterials, and optics.

Materials and Methods

Optical Apparatus. The femtosecond laser source is a mode-locked Ti:sapphire ultrafast oscillator (Chameleon Vision-S; Coherent Inc.) with a central wavelength of 800 nm, a pulse width of 75 fs, and a repetition rate of 80 MHz. The reflective liquid-crystal SLM (Pluto NIR-2; Holoeye Photonics AG) has 1,920 × 1,080 pixels, with pixel pitch of 8 μm, on which computer-generated holograms with 256 gray levels can be displayed. The sample was mounted on a nanopositioning stage [E545; Physik Instrumente (PI) GmbH & Co. KG] with nanometer resolution and a three-dimensional 200- × 200- × 200-μm moving range to precisely locate microstructures under optical microscopy.

Geometry of Chiral Microstructures. To define chiral microstructures using two-photon polymerization, we exploited the following parameterization in Cartesian coordinates:

$$\Omega(\varphi, R, \delta) = \begin{pmatrix} x(\varphi, R, \delta) \\ y(\varphi, R, \delta) \\ z(\varphi, R, \delta) \end{pmatrix} = \begin{pmatrix} \sqrt{R^2 + \delta^2} \times \cos[\pm\varphi + \tan^{-1}(\delta/R)] \\ \sqrt{R^2 + \delta^2} \times \sin[\pm\varphi + \tan^{-1}(\delta/R)] \\ H\varphi/2\pi \end{pmatrix} \begin{matrix} \varphi \in [0, 2\pi] \\ R \in [0, D/2] \\ \delta \in [-\delta_0/2, \delta_0/2] \end{matrix},$$

[3]

which defines right-handed (+) and left-handed (−) microstructures of diameter D, cross-sectional width $\delta_0 = 2\mu m$, and helical pitch H.

Sample Preparation and Characterization. A commercially available zirconium–silicon hybrid sol-gel material (SZ2080), provided by IESL-FORTH, was used in our experiments. The prebaking process was set to a thermal platform at 100 °C for 45 min in order to evaporate the solvent in the SZ2080. After polymerization illuminated by the femtosecond laser, the sample was developed in 1-propanol for half an hour until the portion without polymerization was washed away. The scanning electron microscopy (SEM) images were taken with a scanning electron microscope (ZEISS EVO18) operated at an accelerating voltage of 10 keV after depositing a ~10-nm gold layer.

Preparation of Chemicals. Enantiomers L-phenylalanine and D-phenylalanine (p2126 and p1751, ≥98%; Sigma-Aldrich) were dissolved in deionized water and formed solutions with concentration of 1 mg·mL⁻¹. The solution with a volume of 0.1 mL was dropped on the chiral microstructures for collecting the VDS spectra of corresponding enantiomers. The sample was used for multiple measurements. After each measurement, the sample was immersed in deionized water for removing excess chiral molecules.

Details of the Experiment Measuring VDS Spectrum. After positioning the chiral microstructure to the center of optical vortex, the scattering intensity profiles by addressing their topological charges were caught by the CCD (Panasonic WV-BP334 camera having 768 × 576 pixels with an acquisition time of 500 ms). To avoid introducing extrinsic chirality from light, we carefully tuned the optical setup to achieve nearly normal incidence with the tilting angle smaller than 1°. The vortex beams are aligned to chiral microstructures with the transverse precision of 0.5 μm (~3% compared to the structure diameter) by a nanopositioning stage, which maintains a large and robust chiroptical response. The deviations in our experiments arise from mechanical vibration, which includes the axial misalignment and slanted incidence. The laser power measured after the iris was 0.5 mW for clarity of the optical images. These optical images were gathered over 30 min per measurement of a chiral microstructure. This approach excludes time-dependent effects from the measured signals, showing the robust behavior.

Numerical Simulation of Field Distribution under the Objective. Under the paraxial approximation, the electric field of an optical vortex beam can be described as

$$\boldsymbol{E}_\ell^{in}(r, \varphi, z) = \sqrt{\frac{2}{\pi\omega^2(z)|\ell|!}} \left(\frac{\sqrt{2}r}{\omega(z)}\right)^{|\ell|} \exp\left(-\frac{r^2}{\omega^2(z)}\right) \exp(i\ell\varphi)\boldsymbol{E}_{\boldsymbol{x}},$$

[4]

where $\omega(z)$ is the radius of beam, $\boldsymbol{E}_{\boldsymbol{x}} = E_x \cdot \hat{\boldsymbol{x}}$ is the horizontal polarization vector, and r, φ, and z are the cylindrical coordinates. When the beam waist (where $z = 0$ in Eq. 4) is located at the back-aperture plane of an objective lens with numerical aperture 0.9, the electric field distribution on the focal plane can be simulated by using vectorial Debye diffraction theory (41, 42):

Table 1. Comparison of CDS and VDS responses on chiral microstructures with different diameter D

	D, μm					
	11.5	13.4	15.2	17.3	19.5	21.2
λ of CDS peak, μm	21.7	23.6	25.4	27.5	29.7	31.4
λ of VDS peak*, μm	0.8	0.8	0.8	0.8	0.8	0.8
CDS ($\lambda = 0.8$ μm)	Negligible signals ($|\ell|\equiv 0$)					
VDS ($\lambda = 0.8$ μm)†	117% ($|\ell| = 16$)	113% ($|\ell| = 20$)	121% ($|\ell| = 26$)	114% ($|\ell| = 26$)	114% ($|\ell| = 30$)	116% ($|\ell| = 34$)

*The simulated CDS peak is red-shifted by increasing the diameter D of chiral microstructures. The VDS peak is right-shifted on topological charge $|\ell|$ with larger chiral microstructures.

†At the wavelength of 800 nm, gigantic VDS values can still provide distinct optical chirality of microstructures, whereas CDS measurements have negligible signals.

$$\vec{E}(r_2, \varphi_2) = iC \begin{bmatrix} \hat{x} & \hat{y} & \hat{z} \end{bmatrix} \iint_\Omega sin(\theta) E_\ell^{in}(\theta, \varphi) \sqrt{cos\theta} \begin{bmatrix} 1 + (cos\theta - 1)cos^2\varphi \\ (cos\theta - 1)cos\varphi\,sin\varphi \\ sin\theta\,cos\varphi \end{bmatrix}$$

$$exp\{ikr_2 sin\theta cos(\varphi - \varphi_2)\}d\theta d\varphi \qquad [5]$$

where $\vec{E}(r_2, \varphi_2)$ is the electric field vector, (r_2, φ_2) are the polar coordinates at the focal plane, C is a constant, θ is the convergence angle of the objective, and k is the wavenumber of light.

Data Availability. All study data are included in the paper and *SI Appendix*.

1. K. Y. Bliokh, F. J. Rodriguez-Fortuno, F. Nori, A. V. Zayats, Spin-orbit interactions of light. *Nat. Photonics* **9**, 796–808 (2015).
2. J. H. Poynting, The wave motion of a revolving shaft, and a suggestion as to the angular momentum in a beam of circularly polarised light. *Proc. R. Soc. Lond. A Contain. Pap. Math. Phys. Character* **82**, 560–567 (1909).
3. L. Allen, M. W. Beijersbergen, R. J. C. Spreeuw, J. P. Woerdman, Orbital angular momentum of light and the transformation of Laguerre-Gaussian laser modes. *Phys. Rev. A* **45**, 8185–8189 (1992).
4. D. G. Grier, A revolution in optical manipulation. *Nature* **424**, 810–816 (2003).
5. J. Wang et al., Terabit free-space data transmission employing orbital angular momentum multiplexing. *Nat. Photonics* **6**, 488–496 (2012).
6. M. P. J. Lavery, F. C. Speirits, S. M. Barnett, M. J. Padgett, Detection of a spinning object using light's orbital angular momentum. *Science* **341**, 537–540 (2013).
7. M. Hentschel, M. Schäferling, X. Duan, H. Giessen, N. Liu, Chiral plasmonics. *Sci. Adv.* **3**, e1602735 (2017).
8. Y. Zhao et al., Chirality detection of enantiomers using twisted optical metamaterials. *Nat. Commun.* **8**, 14180 (2017).
9. J. K. Gansel et al., Gold helix photonic metamaterial as broadband circular polarizer. *Science* **325**, 1513–1515 (2009).
10. V. K. Valev, J. J. Baumberg, C. Sibilia, T. Verbiest, Chirality and chiroptical effects in plasmonic nanostructures: Fundamentals, recent progress, and outlook. *Adv. Mater.* **25**, 2517–2534 (2013).
11. W. Chen et al., Nanoparticle superstructures made by polymerase chain reaction: Collective interactions of nanoparticles and a new principle for chiral materials. *Nano Lett.* **9**, 2153–2159 (2009).
12. A. Kuzyk et al., DNA-based self-assembly of chiral plasmonic nanostructures with tailored optical response. *Nature* **483**, 311–314 (2012).
13. X. Shen et al., Rolling up gold nanoparticle-dressed DNA origami into three-dimensional plasmonic chiral nanostructures. *J. Am. Chem. Soc.* **134**, 146–149 (2012).
14. J. Kumar et al., Detection of amyloid fibrils in Parkinson's disease using plasmonic chirality. *Proc. Natl. Acad. Sci. U.S.A.* **115**, 3225–3230 (2018).
15. E. Hendry et al., Ultrasensitive detection and characterization of biomolecules using superchiral fields. *Nat. Nanotechnol.* **5**, 783–787 (2010).
16. Y. Tang, A. E. Cohen, Enhanced enantioselectivity in excitation of chiral molecules by superchiral light. *Science* **332**, 333–336 (2011).
17. W. J. Choi et al., Terahertz circular dichroism spectroscopy of biomaterials enabled by kirigami polarization modulators. *Nat. Mater.* **18**, 820–826 (2019).
18. J. Mun et al., Electromagnetic chirality: From fundamentals to nontraditional chiroptical phenomena. *Light Sci. Appl.* **9**, 139 (2020).
19. M. Babiker, C. R. Bennett, D. L. Andrews, L. C. Dávila Romero, Orbital angular momentum exchange in the interaction of twisted light with molecules. *Phys. Rev. Lett.* **89**, 143601 (2002).
20. W. Loffler, D. J. Broer, J. P. Woerdman, Circular dichroism of cholesteric polymers and the orbital angular momentum of light. *Phys. Rev. A* **83**, 065801 (2011).
21. W. Brullot, M. K. Vanbel, T. Swusten, T. Verbiest, Resolving enantiomers using the optical angular momentum of twisted light. *Sci. Adv.* **2**, e1501349 (2016).
22. M. Esposito et al., Triple-helical nanowires by tomographic rotatory growth for chiral photonics. *Nat. Commun.* **6**, 6484 (2015).
23. B. Frank et al., Large-area 3D chiral plasmonic structures. *ACS Nano* **7**, 6321–6329 (2013).
24. A. G. Mark, J. G. Gibbs, T. C. Lee, P. Fischer, Hybrid nanocolloids with programmed three-dimensional shape and material composition. *Nat. Mater.* **12**, 802–807 (2013).
25. M. Esposito et al., Nanoscale 3D chiral plasmonic helices with circular dichroism at visible frequencies. *ACS Photonics* **2**, 105–114 (2014).
26. M. Thiel et al., Polarization stop bands in chiral polymeric three-dimensional photonic crystals. *Adv. Mater.* **19**, 207–210 (2007).
27. X. Li et al., High-efficiency alignment of 3D biotemplated helices via rotating magnetic field for terahertz chiral metamaterials. *Adv. Opt. Mater.* **7**, 1900247 (2019).
28. M. Padgett, J. Courtial, L. Allen, Light's orbital angular momentum. *Phys. Today* **57**, 35–40 (2004).
29. P. McPhie, Circular dichroism studies on proteins in films and in solution: Estimation of secondary structure by g-factor analysis. *Anal. Biochem.* **293**, 109–119 (2001).
30. W. Feng et al., Assembly of mesoscale helices with near-unity enantiomeric excess and light-matter interactions for chiral semiconductors. *Sci. Adv.* **3**, e1601159 (2017).
31. Q. Zhang et al., Unraveling the origin of chirality from plasmonic nanoparticle-protein complexes. *Science* **365**, 1475–1478 (2019).
32. R. Verre et al., Metasurfaces and colloidal suspensions composed of 3D chiral Si nanoresonators. *Adv. Mater.* **29**, 1701352 (2017).
33. G. Kulkarni, R. Sahu, O. S. Magaña-Loaiza, R. W. Boyd, A. K. Jha, Single-shot measurement of the orbital-angular-momentum spectrum of light. *Nat. Commun.* **8**, 1054 (2017).
34. K. Huang et al., Ultrahigh-capacity non-periodic photon sieves operating in visible light. *Nat. Commun.* **6**, 7059 (2015).
35. J. E. Curtis, D. G. Grier, Structure of optical vortices. *Phys. Rev. Lett.* **90**, 133901 (2003).
36. Y. Tang, A. E. Cohen, Optical chirality and its interaction with matter. *Phys. Rev. Lett.* **104**, 163901 (2010).
37. J. García-Guirado, M. Svedendahl, J. Puigdollers, R. Quidant, Enantiomer-selective molecular sensing using racemic nanoplasmonic arrays. *Nano Lett.* **18**, 6279–6285 (2018).
38. K. A. Forbes, D. L. Andrews, Spin-orbit interactions and chiroptical effects engaging orbital angular momentum of twisted light in chiral and achiral media. *Phys. Rev. A* **99**, 023837 (2019).
39. K. A. Forbes, D. L. Andrews, Optical orbital angular momentum: Twisted light and chirality. *Opt. Lett.* **43**, 435–438 (2018).
40. H. E. Lee et al., Amino-acid- and peptide-directed synthesis of chiral plasmonic gold nanoparticles. *Nature* **556**, 360–365 (2018).
41. J. Ni et al., Three-dimensional chiral microstructures fabricated by structured optical vortices in isotropic material. *Light Sci. Appl.* **6**, e17011 (2017).
42. X. Li, T.-H. Lan, C.-H. Tien, M. Gu, Three-dimensional orientation-unlimited polarization encryption by a single optically configured vectorial beam. *Nat. Commun.* **3**, 998 (2012).

Ni et al.
Gigantic vortical differential scattering as a monochromatic probe for multiscale chiral structures

PNAS | 7 of 7
https://doi.org/10.1073/pnas.2020055118